

Fault slip rates for the active External Dinarides thrust-and-fold belt

Vanja Kastelic¹ and Michele Matteo Cosimo Carafa¹

(1) Istituto Nazionale di Geofisica e Vulcanologia -INGV, Sezione di Sismologia e Tettonofisica, Via di Vigna Murata 605, 00143 Rome, Italy.

E-mail: vanja.kastelic@ingv.it; michele.carafa@ingv.it

ABSTRACT

We present estimates of slip rates for active faults in the External Dinarides. This thrust-and-fold belt formed in the Adria - Eurasia collision zone by the progressive formation of NE-dipping thrusts in the footwalls of older structures. We calculated the long-term horizontal velocity field, slip rates and related uncertainties for active faults using a thin-shell finite element method. We incorporated active faults with different effective fault frictions, rheological properties, appropriate geodynamic boundary conditions, laterally varying heat flow and topography. The results were obtained by comparing the modeled maximum compressive horizontal stress orientations with the World Stress Map database. The calculated horizontal velocities decrease from the southeastern External Dinarides to the northwestern parts of the thrust-and-fold belt. This spatial pattern is also evident in the long-term slip rates of active faults. The highest slip rate was obtained for the Montenegro active fault, while the lowest rates were obtained for active faults in northwestern Slovenia. Low slip rates, influenced by local active diapirism, are also characteristic for active faults in the offshore central External Dinarides. These findings are contradictory to the concept of Adria as an internally rigid, aseismic lithospheric block because the faults located in its interior release a part of the regional compressive stress. We merged the modeling results and available slip rate estimates to obtain a composite solution for slip rates.

Key words: fault slip rate, active fault, External Dinarides, rheology, seismic hazard

1. INTRODUCTION

The long-lived compressional eastern contact between Adria and Eurasia has formed and consequently deformed the Dinarides thrust-and-fold belt. In its polyphase evolution since the Late Jurassic, the convergence was first expressed by formation of the Internal Dinarides [Tari, 2002]. Thrusting gradually propagated westward with the migration of foredeep basin sequences in front of the growing belt and over platform carbonates since the Late Cretaceous – Early Paleogene [Tari, 2002; Korbar, 2009], forming the External Dinaric thrust belt (Figure 1). The oldest foredeep flysch rocks of the External Dinarides are located in its northwestern part (western Slovenia) and have Early Eocene ages [Drobne and Pavlovec, 1991]. The onset of flysch deposition in the foredeeps gets progressively younger towards the southeast along the thrust belt and offshore towards the west [Tari, 2002]. The flysch rocks in the present day coastal and island areas formed during the Priabonian age [Marjanac et al., 1998], while in the offshore Adriatic the foredeep basins progressively formed during the Oligocene-Miocene [Tari-Kovačić, 1998; Tari-Kovačić et al., 1998].

The Central Adriatic, referred to as the Middle Adriatic Ridge by some authors [e.g., Scisciani and Calamita, 2009], is interpreted as a linkage zone between the Apennine and Dinaric thrust belt [e.g., Scisciani and Calamita, 2009] or as a foreland deformation zone [Gambini et al., 1997; Argnani, 1998]. In the present structural setting, the Central Adriatic is characterized by compressionaly reactivated Permian-Triassic normal faults [Boccaletti et al., 2005; Scisciani and Calamita, 2009], external SW-dipping Apennine [Scrocca, 2006] and NE-dipping External Dinarides thrusts [Grandić and Markulin, 2000; Herak et al., 2005; Fantoni and Franciosi, 2010] (Figure 2). Active faults in this region deform late-Quaternary deposits and generate local submerged uplifts [Scisciani and Calamita, 2009]. The spatial extension of the Middle Adriatic Ridge is closely related to the occurrence of halokinetic structures [Geletti et al., 2008; Del Ben et al., 2010] and active thrusting

is accompanied by evaporate diapirism that deforms the youngest Pliocene-Quaternary sediments [Grandić et al., 1999; Finetti and Del Ben, 2005; Herak et al., 2005; Geletti et al., 2008].

The terminology describing the Dinarides is not always consistent and different terms such as “Western Dinaric thrust belt” [Tari, 2002] and “External Dinarides” [Korbar, 2009] are used to describe the same units. We define the term “External Dinarides” (ED) for the SW-verging thrust belt formed along the Eastern Adria margin and the NE dipping thrusts of the Central Adriatic. This implies the ED developed within both the Dinaric (Eurasia) and Adriatic lithosphere. The ED include the “central and western parts of the Western Dinaric thrust belt and Eastern Adria imbricated structures” units described by Tari [2002] and the “External Dinarides and eastern part of the Adriatic foredeep” units defined by Korbar [2009].

The neotectonic fault activity in the External Dinarides is demonstrated by displaced Quaternary units [Geletti et al., 2008], GPS data [Bennett et al., 2008; Devoti et al., 2008] and earthquakes [eg. Ribarič, 1979; Herak et al., 1995; Albini, 2004]. Seismic deformation in the ED is released through medium-to-large seismic events [Herak et al., 1995; Herak et al., 1996; Stucchi et al., 2007]. In the Central Adriatic, thrust fault seismicity is related to compression release on the NE dipping faults [Markušić et al., 1990; Herak et al., 2005] without any current compressive stress by the Apennine thrust front [Del Ben et al., 2010]. The active faults in the ED have hosted some of the strongest earthquakes of the northern Mediterranean region: the M 7.2 1667 Dubrovnik earthquake [Papazachos et al., 2009], the 1979 M_w 7.1 Montenegro earthquake [Benetatos and Kiratzi, 2006], the 1511 M 6.8 western Slovenia earthquake [Ribarič, 1982] and the 1639 M 6.8 southern coastal Croatia earthquake [Papazachos et al., 2009] (Figure 1).

The evolution and activity of the ED indicate that individual thrusts accommodate the compression simultaneously. Koyi et al. [2000] suggested this scenario for thrust belts evolving over a low-

friction decollement. In such conditions, older faults remain active when new thrusts form in front of them. Therefore, for any given percentage of bulk shortening, the slip rate along individual thrusts is relatively low, but they remain active as long as the boundary conditions and stress field are unchanged. The low-friction decollements in the ED are the Permian shales locally interbedded with gypsum, fine-grained Early-Mid Triassic clastic rocks and Late Jurassic-Early Cretaceous anhydrites [Tari, 2002; Velaj, 2002]. The presence of such low-viscosity layers in the ED shows the importance of rheology in the evolution of thrust-and-fold belts. The vertical variations of rheology among different lithological units control the thrust propagation [Suppe et al., 2009], whereas the laterally varying vertically integrated lithospheric strength controls deformation on a regional scale [Lankreijer et al., 1997]. Previous rheological studies determined higher lithospheric strengths for Adria with respect to surrounding areas such as the Dinarides [Tesauro et al., 2009; Carafa and Barba, 2011]. After examining the distribution of shallow earthquakes, Anderson and Jackson [1987] suggested that the seismic deformation was mainly released in areas surrounding a relatively aseismic and rigid Adriatic block. Several geodetic analyses of GPS measurements for circum-Adriatic data used the Anderson and Jackson assumption to determine alternative poles of rotation for the Adria microplate. Recently, Devoti et al. [2008] claimed that the high variability of GPS measurements indicates that Adria is not moving as a rigid plate. According to the same study, none of the block subdivisions of Adria seem to adequately represent the complexity of Adriatic kinematics. Several earthquake sequences show that the recent seismicity of Adria is comparable to the seismicity of several well-known earthquake-prone areas in the circum-Adriatic region [Markusić et al., 2008].

Despite the fact that geological data, GPS measurements and seismicity show the ED to be an active thrust belt, just little research on better understanding the rheological setting and slip rates of active faults is available. Recently a series of finite element methods have been applied to study active tectonics of the Central Mediterranean, revealing the importance of mantle flow in predicting

crustal stress patterns [Barba et al., 2008; Ismail-Zadeh et al., 2010] as well as the kinematic behaviour of faults [Howe and Bird, 2010], but none of them addressed the ED in detail.

We focus on determining slip rates for active faults in the External Dinarides. We investigated the effect of uncertainties in Adria-Eurasia compression, lithosphere structure and rheology on slip rates. We applied the finite element method, which is especially valuable for modeling blind thrust faults with limited geological exposure and faults located offshore or in poorly surveyed areas. The geometries of active faults with variable effective fault frictions were used as input data in the modeling procedure. In total, we obtained 13,824 models, taking into consideration uncertainties in lithosphere structure, rheological parameters and boundary conditions. The horizontal velocity field, maximum compressive horizontal stress orientations and the fault slip rates were computed for each model. We scored the model-predicted maximum compressive horizontal stress axes (SHmax) against the World Stress Map database release 2008 [Heidbach et al., 2008]. The best-fitting models were averaged to give final values of horizontal velocity, stress azimuth and long-term slip rates.

The highest average slip rate of 2.01 mm/yr was calculated for the thrust in the southeastern part of the ED. The slip rates diminish to the northwest and are lower than 0.15 mm/yr for the northwesternmost faults. Low, but significant, slip rates were found also for the most external faults, which are located in the strong, but fragmented, Adriatic lithosphere. These results contrast the idea of Adria being a unique block without internal deformation. For active fault slip rates in the ED, we introduce a composite solution obtained by combining our modeling results with available estimates for active faults in the region.

2. METHOD

We introduced 20 active faults in the area from northwestern Slovenia to the coastal and offshore areas of southern Croatia and Montenegro (Figure 3). The finite element program SHELLS (Bird [1999], version of April 11th, 2005) was used to calculate slip rates for active faults. This code computes the lithospheric horizontal velocity field based on boundary conditions and rheology. It incorporates faults and rheological characteristics in a two-layer crust and lithospheric mantle mesh with laterally varying thickness, heat flow and topography. We built several models to properly analyze the effects of input parameter uncertainties on slip rates. The physical and numerical values used in our modeling and not described in section 2.2 are the same as in the Earth5-049 model of Bird et al. [2008].

2.1. Active faults

The active fault data included in our model originate from the revision of available literature geologic [Ivančić et al., 2006; Kastelic et al., 2008; Kralj and Tomljenović, 2009], earthquake [Herak et al., 1995; Herak et al., 1996; Bajc et al., 2001; Kastelic et al., 2008] and seismotectonic [Kuk et al., 2000] data. The active faults were constrained also by considering the available structural and geological information [Benac et al., 2004; Grandić et al., 2007; Benac et al., 2008; Geletti et al., 2008], regional geodynamic studies [Grenerczy et al., 2005; Caporali et al., 2009] and field observations and measurements. Using this approach, we checked for the geometric and kinematic coherence of each active fault in the ED. These active faults are part of the Database of Individual Seismogenic Sources - DISS database - in the form of composite seismogenic sources [Basili et al., 2008], versions DISS 3.1.0 [DISS Working Group, 2009] and DISS 3.1.1 [DISS Working Group, 2010], where neighboring active faults not included in this work are represented. Each of the modeled active faults represents the leading fault plane capable of releasing stress through moderate-to-strong earthquakes.

To separate the modeled faults from those not considered in this study, we introduced the AD1 edge (Figure 4). This boundary delimits the modeled ED faults from neighboring faults in the Southern Alps in the northwest of the model and the External Apennines in the west and southwest of the model (Figure 4). The distinction between the ED and active Southern Alps faults is in their kinematics and strike; in the ED model, the faults with the prevailing NW-SE dextral strike-slip and strike were included, while the E-W Southern Alps thrusts were omitted. In the Central Adriatic, we modeled the seismically active NE-dipping thrusts as part of the ED and did not include the external thrusts of the Apennine thrust belt (Figure 4). In the southeast, we included the NW-SE striking faults offshore of Montenegro, but not the NNE-SSW striking faults belonging to the Albanides. This choice is consistent with the structural and geological differences between these areas.

A common characteristic of the active faults introduced throughout the entire investigated area is their general NW-SE orientation (Figure 3; Table 1). The active faults that diverge most from this regional trend are located in the central part of the ED and have average strikes of 285° and 295° . We report the detailed geometries and kinematic characteristics of these faults in Table 1 and Figure 3. To capture the geological and structural variations, we divided the ED into three principal zones (Figure 3):

- Zone A represents the northwesternmost part of the ED and corresponds to its oldest active part (Tari, 2002). Faults located in this zone have become progressively steeper-dipping during the evolution of the ED. Currently, they are steep to subvertical and are active as strike-slip faults (Kastelic et al., 2008). Their longevity, total bulk displacement and reactivation suggest they are weak structures [Faulkner and Rutter, 2001; Imber et al., 2008]. Zone A contains five active faults identified with the suffix A (Table 1).
- Zone B represents the largest part of the ED and comprises the islands, coastal and inland areas of its central and southern parts. This zone is “intermediate” in terms of evolution of the belt and related bulk fault displacement. The inner active faults show the steepest dips.

The faults in the coastal and island areas are characterized by lower dip angles, while dips become even shallower for the southeasternmost faults. The majority of the externally positioned faults behave as thrusts, while the internal faults have a strike-slip component. Seismogenic release of stress is evident throughout the entire width of this zone [Kuk et al., 2000]. Zone B contains 12 active faults identified with the suffix B.

- Zone C occupies offshore areas of the ED and extends over the eastern and central parts of Adria. Within the westwards migration of the Adria – Eurasia convergence, zone C developed after the internal parts of the ED [Tari, 2002] and, thus, the three zone C faults (identified with the suffix C) have younger ages and lesser bulk displacement than those in zones A and B. These faults exhibit shallow-to-medium dips, with dip-slip motion as shown by focal mechanisms [Herak et al., 2005; Herak et al., 1995].

The most external active faults of our model (AF16C, AF17C and parts of AF15C) are positioned in the Central Adriatic, area referred to as the Middle Adriatic Ridge (e.g., Scisciani and Calamita, [2009]). We did not model the smaller thrust couples with opposing dips in this area [Scisciani and Calamita, 2009] as we interpret the leading, seismically active thrusts to be the NE dipping planes (AF16C). This interpretation was performed by combining geological, geophysical, seismological studies [Grandić and Markulin, 2000; Herak et al., 2005; Scrocca et al., 2006; Geletti et al., 2008; Scisciani and Calamita, 2009; Del Ben et al., 2010; Fantoni and Franciosi, 2010]. Faults to the west of our model [e.g., Scrocca, 2006] lie nearby, but do not intersect nor exclude the seismically active faults included in our model.

Following the approach of Bird [1996], we preferred to possibly overestimate the active fault length than exclude poorly studied or buried fault sections. If such faults were not favorably oriented within the present stress field, they would remain inactive in the model simulations and would have no effect on the final solution. Moreover, if such faults resulted in very high slip rates, the solution

would not be supported by the World Stress Map (WSM) stress orientations and the model would be rejected. Setting the length of the Eastern-Adriatic offshore fault (AF15C) was challenging due to its being entirely offshore and its dimensions are not covered by the available data not covering the entire dimensions of the fault. Based upon the available data and following the above rationale, we compiled AF15C fault as presented in Table 1 and Figure 3. We did not account for secondary structures or minor fault splays, as they accommodate displacement along the leading fault plane. Minor faults and splays were not included in the mesh due to their narrow spacing. The current knowledge and data availability do not allow a more precise segmented fault model and the active faults introduced here best capture the deformation. Additional modeled faults might influence the calculated fault slip rates. This issue is addressed by reporting the continuum strain rate map of the investigated area, where the strain of the potentially missing active faults is compensated by the anelastic strain rates of continuum elements.

2.2. Finite Element Model (FEM)

2.2.1. Mesh

The constructed mesh (Figure 4) consists of 4,794 triangular-prism continuum elements with an average area of 82 km² and 171 planar fault elements with an average length of 13 km that represents the 20 active faults described in section 2.1. The edges of the model are far enough from the ED to avoid any boundary effects. We present the results east of the AD1 internal model boundary (Figure 4). Showing results for the entire grid could be misleading as we did not include geological data nor did we model the geodynamics for the Apennines and Southern Alps that bound the modeled region. The mesh was defined in three dimensions with regards topographic elevation, crustal thickness, heat flow and upper mantle lithospheric thickness. Vertical values were determined using 1 km steps at each of the seven Gauss integration points of each finite element

(continuum or fault). Surface topography was taken from the global ETOPO1 Global Relief Model with a 1'x 1' cell size [Amante et al., 2009].

Crustal thicknesses and related uncertainties were taken from Grad et al. [2009] and were used to construct three maps: CRUS1, the minimum crustal thickness map; CRUS2, the average crustal thickness map; and CRUS3, the maximum crustal thickness map. We built three meshes, each with the corresponding value of the appropriate crustal thickness map assigned to each node. The thermal regime at the modeled depths was calculated assuming steady state vertical conductive heat flow. We digitized surface heat flow density maps from Milivojević [1993], Del Ben et al. [1994], Della Vedova et al. [2001] and Cloetingh et al. [2005] and merged them into a unique heat flow map. Della Vedova et al. [2001] modeled the undisturbed steady state surface conductive heat flow of Italy and surroundings, obtaining values higher than 0.045 W/m^2 for the Adriatic and its foreland. Surface heat flow values below this value are attributed to the effects of groundwater convection and high sedimentation rates [Fowler et al., 1998; Della Vedova et al., 2001]. We applied these findings by discarding heat flow values lower than the 0.045 W/m^2 from the heat flow map. To ensure realistic thermal conditions, we also adjusted the upper heat flow bounds by setting the upper lithosphere temperature limit at 1,673 K because at this temperature, minerals have low viscosities more typical for the asthenosphere than for the lithosphere. Based on the upper temperature limit, we manually corrected heat flow values for those nodes with a temperature at the base of the crust greater than 1,673 K (a total of 32 nodes for the mesh reproducing crustal model CRUS3). For such nodes, the upper mantle lithospheric thickness was imposed as two km, whereas the lithosphere upper mantle thickness for the remaining nodes was calculated from the surface heat flow data, assuming steady state vertical conduction and the upper temperature limit at the base of the lithosphere of 1,673 K. This method for determining the thermal regime at depth can be affected by uncertainties, such as those due to thermal conductivity or radiogenic heat production. Therefore, we defined an arbitrary uncertainty of 10% to the obtained heat flow map. For each node in the

three meshes with different crustal thicknesses, we assigned three heat flow hypotheses: HEAT1, the average heat flow minus 5% of its value; HEAT2, the average heat flow value; and HEAT3, the average heat flow plus 5%. Considering different crustal structures and heat flow maps resulted in nine final meshes, adequately representing uncertainties in the lithospheric thickness and thermal regime.

We did not assume an isostatic balance for any of the mesh elements, as we considered a low positive pressure at the base of the lithosphere to be more appropriate for the Adria and ED geodynamic setting. In the nine meshes, we calculated the average pressure anomaly over the whole lithosphere to be $11.29 \pm 8.28 \text{ kg/m}^3$. According to the various scenarios proposed for Central Mediterranean geodynamics, this positive pressure anomaly is due to slab rollback or mantle corner flow [Faccenna and Becker, 2010].

2.2.2. Boundary conditions

To reproduce the regional geodynamic setting, we divided the model edge into three parts: EU, AL and AD. We modeled all boundary conditions as residual horizontal velocities with respect to a fixed Eurasia. Based on the GPS measurements and derived velocity models [Grenerczy et al., 2005; Caporali et al., 2009; Caporali et al., 2011], we set the EU edge fixed with respect to Eurasia. For the AL edge, we fixed velocities at 2.2 mm/yr oriented N175, as measured for the western part of the Macedonian block with respect to stable Eurasia [Burchfiel et al., 2006]. More detailed conditions were needed to model the AD edge. This edge was set with a considerable distance from the External Dinarides to avoid boundary effects on the results from choosing AD1 as the external ED border (Figure 4). We applied 16 sets of horizontal velocities to the AD nodes to reproduce the calculated values and their relative uncertainties from Barba et al. [2008] on the AD1 edge (Figure 4). This model has a 1.64 mm/yr horizontal velocity root mean square (RMS) with respect to the GPS datasets [Caporali, 2007; Devoti et al., 2008]. To compensate for this difference, we assigned a

+/- 1 mm/yr error to the northern and the eastern component of the AD1 nodes. We divided the error into 0.5 mm/yr steps, thus resulting in 16 datasets of AD1 horizontal velocities. For each velocity dataset, we calculated the corresponding AD1-Eurasia rotation poles and used these to obtain 16 sets of boundary conditions for the AD edge. By applying these boundary conditions to the mesh, we appropriately modeled only the area to the east of AD1.

2.2.3. Rheology

We applied the same mathematical formulation for the rheological conditions to all model elements, allowing deformation to occur as frictional sliding, nonlinear dislocation creep or pure plastic creep. For each triangular prism element in the mesh, we calculated the frictional faulting and dislocation creep shear stresses at a given fixed strain rate and at 1 km depth intervals. We set a constant plasticity limit of 500 MPa following Bird [1989] and Bird et al. [2008]. The minimum of these three values was the shear stress assigned to a particular depth of the triangular prism element. For each element, the shear stress integral across the lithosphere thickness represents the strength envelope and, thus, the resistance to deformation [Bird, 1989; Carafa and Barba, 2011]. Below we briefly describe the rheological characteristics of our model.

2.2.3.1 Dislocation creep

For each node at crustal and mantle depths, the dislocation creep (power law) rheology is given by:

$$\tilde{\sigma} = 2 \cdot \left[2A_{C,M} \cdot \left(2\sqrt{-\dot{\epsilon}_1\dot{\epsilon}_2 - \dot{\epsilon}_1\dot{\epsilon}_3 - \dot{\epsilon}_2\dot{\epsilon}_3} \right)^{\frac{(1-n)}{n}} \exp\left(\frac{B_{C,M} + C_{C,M}z}{T}\right) \right] \tilde{\dot{\epsilon}} \quad (1)$$

where $\tilde{\sigma}$ is the shear stress, $\tilde{\dot{\epsilon}}$ is the anelastic strain rate tensor, $\dot{\epsilon}_1, \dot{\epsilon}_2$ and $\dot{\epsilon}_3$ are its three eigenvalues, T is the absolute temperature and $A_{C,M}$, $B_{C,M}$, and $C_{C,M}$ represent the rheological

parameters of the crust and mantle. Varying $B_{C,M}$ changes the strength characteristics of both the crust and mantle. Due to limited knowledge of fluid pore pressure and mineral composition for the study area, we tested six B_C values for the crust and eight B_M values for the mantle, with all remaining rheological and thermal parameters taken from the EARTH5-49 model [Bird et al., 2008]. We reproduced the laboratory power law creep rheologies by using the $B_{C,M}$ values listed in Table 2. The range of tested crustal rheologies varies from Westerly granite to dry diabase and the tested range for the mantle varies from wet dunite [Karato, 1984; Watts, 2001] to diopside [Dimanov and Dresen, 2005]. Combining the crustal and mantle rheologies produced 48 pairs of crust-mantle power law creep rheologies.

2.2.3.2 Fault rheology

Brittle faulting in a rock volume is defined by the external critical shear stress exceeding the strength of the rock volume:

$$\sigma_f = \mu_f (\sigma_n - P_w), \quad (2)$$

where σ_f is the frictional shear stress, σ_n is the normal stress component, μ_f is the coefficient of initial friction and P_w is the pore pressure in the rock volume.

The SHELLS code differentiates between fault friction and the continuum friction coefficient, which is set at 0.85. The initial fault friction coefficient was set at 0.6 [Scholz, 1998] and we introduced variations in effective fault friction by modifying the equation of Geist and Andrews [2000]:

$$\mu_{eff(i)} = \mu_f \left(1 - \frac{FA_{(i)}}{FA_{max}} \right), \quad (3)$$

where $\mu_{eff(i)}$ is the effective fault friction value for each fault element, μ_f is the initial fault friction value, FA_{max} is the maximum displacement of the oldest long-lived thrusts and $FA_{(i)}$ is the displacement of the i -th fault element. Different studies show that the mature active faults appear to be weaker and have lower fault friction values than predicted by theoretical studies. Several phenomena can explain mechanical weakness of mature faults: elevated fluid pressure [Faulkner and Rutter, 2001], the presence of phyllosilicates or clays in the fault zone [Imber et al., 2001; Collettini and Holdsworth, 2004], dynamic weakening [Melosh, 1996] or a combination of these causes. In equation (3), $\frac{FA_{(i)}}{FA_{max}}$ introduces fault longevity into the fault friction value and relates it

to the cumulative displacement over geologic time. This ratio does not distinguish among the causes for mechanical weakness of mature faults, but it does provide an opportunity to test if fault weakening is an important parameter in dynamic modeling. As we have not found any indication of mechanical weakness playing a major role in the geodynamics of the ED, we tested two scenarios.

In the first, we set $\frac{FA_{(i)}}{FA_{max}}$ to zero for all the modeled fault elements, while the second scenario

represents a variable $\frac{FA_{(i)}}{FA_{max}}$ considering fault age and the total fault displacement over geological

time. Because no direct measurements or estimates of fault displacement for the ED were available, we utilized the analogue modeling results of Koyi et al. [2000]. Their models of active in-sequence thrusting show an order of magnitude difference in displacement along four active thrusts of different ages in a growing thrust belt above a low-friction decollement. In the direction of thrust belt propagation, the younger external thrusts typically display lower dip angles than the older, internally based faults. As such findings are compatible with the geological evolution and the

geometry of the ED belt, we used them to infer a first approximation of the bulk displacement of active faults in the ED. To incorporate these findings into the model, we assigned each of the three zones defined in section 2.1 a characteristic $\frac{FA_{(i)}}{FA_{\max}}$ value, giving each of the active faults in a particular zone its own $\frac{FA_{(i)}}{FA_{\max}}$ value. We assigned a $\frac{FA_{(i)}}{FA_{\max}}$ value of 0.2 to the youngest active thrusts located in Zone C (Figure 5). For faults located in Zone B, which has a geological evolution comparable to the second oldest thrust in the model of Koyi et al. [2000], we assumed a fault displacement 3.5 times higher than the fault displacement in Zone C. We assigned a $\frac{FA_{(i)}}{FA_{\max}}$ value of 0.7 to this group of active faults. Strike-slip faults located in Zone A are the oldest faults in the ED. Based on the displacements for the oldest thrust obtained by Koyi et al. [2000], we assigned a $\frac{FA_{(i)}}{FA_{\max}}$ value of 0.85 to Zone A faults. Such displacement discretization for active faults of different zones within the ED is compatible with the geological evolution of tectonic events described by Ustaszewski et al. [2008]. The selected $\frac{FA_{(i)}}{FA_{\max}}$ values give effective fault friction $\mu_{eff(i)}$ values varying from 0.09 for the active faults in Zone A to 0.18 for faults in Zone B and to 0.48 for the faults in Zone C.

2.3. Model Generation

We produced two main groups of 6,912 models that take all the uncertainties of input parameters into account. The input data representing the lithospheric and geodynamic uncertainties include three heat flow maps, three crustal thicknesses, 16 boundary conditions, six crustal rheologies, eight mantle rheologies and two sets of effective fault friction. For the first group (Group L), $\frac{FA_{(i)}}{FA_{\max}} = 0$ for all active faults, thus assigning the same effective fault friction to all fault elements. For the

second group (Group V), a variable $\frac{FA_{(i)}}{FA_{\max}}$ was assigned to active faults according to their evolution for a growing thrust belt above a low-friction decollement, as described in the previous section.

2.4. Model scoring

The models did not all adequately represent the geodynamic conditions in the ED. To obtain realistic results, we considered only the models that best fit the available geophysical measurements. To do so, we used the WSM database, release 2008, [Heidbach et al., 2008] as other available geophysical data (such as GPS measurements) are unevenly distributed over the ED. In the WSM database, 217 SHmax values exist within the modeled area. One of these records is of A quality (SHmax accurate to within $\pm 15^\circ$), three records are of B quality (SHmax accurate to within $\pm 15^\circ - 20^\circ$), 97 are of C quality (SHmax accurate to within $\pm 20^\circ - 25^\circ$), 82 are of D quality (SHmax accurate to within $\pm 25^\circ - 40^\circ$), nine are of E quality (SHmax accuracy $> \pm 40^\circ$; unreliable data) and 25 records are of S quality (obtained from single focal mechanism inversion).

Because the reliability of data diminishes from quality class A to class E (and S) and the uncertainty in stress azimuth for the D quality data results in questionable tectonic stress orientations [Zoback, 1992; Heidbach et al., 2007], we determined the SHmax misfit $\varepsilon_{m,j}$ for the m-th model as:

$$\varepsilon_{m,j} = \frac{\sum_{n=1}^{n=217} \alpha |\theta_{m,n} - \theta_{WSM,n}|}{n} \quad (4)$$

where $j = l$ for all models in Group L and $j = v$ for all models in Group V. For the various classes, α was set to 4 for A-quality data, 3 for B-quality data, 1 for C-quality data, 0.5 for D-quality data

and 0 for E- and S-quality data. The stress azimuth of the model at a given point where the n -th stress orientation $\theta_{WSM,n}$ of WSM datum is available is $\theta_{m,n}$.

A paired sample t-Test was performed on Group L and Group V to determine if the two mean misfits between the modeled stress orientations and the WMS data are statistically significant. In the case of $\bar{\varepsilon}_{m,l}$ and $\bar{\varepsilon}_{m,v}$ not showing a statistically significant difference or in the case of $\bar{\varepsilon}_{m,l} < \bar{\varepsilon}_{m,v}$, we would use the models of Group L for further calculations. In these two cases, the t-

Test would suggest that $\frac{FA_{(i)}}{FA_{\max}}$ is not an effective parameter for dynamic models of the ED. In the

case of $\bar{\varepsilon}_{m,v} < \bar{\varepsilon}_{m,l}$, the result of the t-Test would suggest a significant impact of $\frac{FA_{(i)}}{FA_{\max}}$ and we

would further consider the Group V models.

Among the models of the “winning” group, we chose only those fulfilling the $\varepsilon_{m,j} \leq \bar{\varepsilon}_{m,j} - \sigma_{\varepsilon}$ condition, where $\bar{\varepsilon}_{m,j}$ and σ_{ε} represent the mean SHmax misfit and its standard deviation. These models were used to further investigate which crustal and mantle rheology results in minimum misfits to the WSM dataset and to obtain the average values of the horizontal surface velocities and stress orientations. For each fault element, considering only the models fulfilling the $\varepsilon_{m,j} \leq \bar{\varepsilon}_{m,j} - \sigma_{\varepsilon}$ condition, we defined the median slip rate value, the minimum slip rate as the 5th percentile value and the maximum slip rate as the 95th percentile value. The minimum slip rate assigned to each active fault is the average of the 5th percentile values for all fault elements, the maximum slip rate is the average of the 95th percentile values, and the average active fault slip rate is the mean value of the medians of its fault elements.

3. RESULTS

3.1. Paired two-tail t-Test

The mean difference between the two datasets ($\bar{\varepsilon}_{m,l} - \bar{\varepsilon}_{m,v}$) was significantly greater than zero, with $t = 85.18$ and two-tail $p = 1.96$, indicating a statistically significant difference between the two model groups. The 95% confidence interval of the mean difference $\bar{\varepsilon}_{m,l} - \bar{\varepsilon}_{m,v}$ was $(1.059^\circ, 1.108^\circ)$, providing evidence that Group V models better reproduce the stress orientation of the WSM data. Based upon these results, the Group L models were discarded from all subsequent calculations.

All 6,912 models of Group V showed $17.12^\circ \leq \varepsilon_{m,v} \leq 42.27^\circ$, with an average misfit value $\bar{\varepsilon}_{m,v}$ of 22.44° and a standard deviation $\sigma_{\bar{\varepsilon}}$ of 3.85° . To produce final results for horizontal surface velocities, stress orientations and slip rates, we considered only the 596 models with $\bar{\varepsilon}_{m,v}$ lower than 18.61° .

3.2. Continuum rheology

Analysis of the best-fitting models allowed us to re-inspect the distribution of the input parameters for the final 596 models. The rheology input parameters that were most frequently represented within the final best models were clinopyroxene (RMAN6=27%) and enstatite (RMAN5=26%) rheologies for the mantle, and wet quartzite (RCRU2=24%) and quartz-diorite (RCRU3=23%) rheologies for the crust (Figure 6). The final best models showed no strong preference with respect to the input heat flow values, resulting in distributions of 34%, 35% and 31% for HEAT1, HEAT2 and HEAT3, respectively.

3.3. Horizontal velocity field

The calculated long-term horizontal velocity field shows a general NE-to-NNE orientation with decreasing magnitudes from the coastal areas of the External Dinarides inland. The highest

horizontal velocities were obtained for the southeastern offshore and coastal parts of our model, reaching values between 4 and 4.5 mm/yr and oriented N010° – N025° (Figure 7). The horizontal velocities oriented N025° decrease to 1.5 - 2 mm/yr in the inland region. In the central portion of the model, the horizontal velocities remain relatively constant throughout the offshore and coastal parts with values between 2.5 – 3.0 mm/yr and oriented N005° – N020°. They noticeably decrease in magnitude to 1 - 1.5 mm/yr inland. Horizontal velocity vectors oriented N350° – N010° with 1.5 – 2.0 mm/yr magnitudes are typical for the offshore and coastal parts of the northwestern ED, while the more inland regions of the northwestern ED have velocities of 1 mm/yr oriented N350° – N005°.

3.4. Horizontal stress direction

The resulting orientation of the maximum compressive horizontal stress axis generally follows the pattern of the velocity field (Figures 7 and 8). At the southeast of the model (Zone B), SHmax has an orientation of N010° – N020° with no significant difference in the orientation between the offshore and inland parts of the model. In the central portion, the offshore areas do not exhibit a significant change in the SHmax orientation, except for the external-central part of Zone B (area of AF13 and AF14), where the orientations approach N040°. With respect to the coastal and offshore parts, the inner region of the central ED (inner part of Zone B) shows SHmax orientations approaching N025° – N035°. Moving further to the northwest (Zone A), SHmax becomes oriented northwards for both offshore and inland zones, approaching N350° – N010°.

3.5. Slip rates

The highest slip rates are for the offshore Montenegro active fault (AF20B). They exceed 2 mm/yr for five of its eight fault elements (Figure 9; Table 1A) and have an average slip rate of 2.01 mm/yr for the entire fault. An average slip rate greater than 1.0 mm/yr was found for at least one fault element of the Metković active fault (AF18B), with a highest average rate of 1.58 mm/yr. The

average rate for the entire fault is 0.98 mm/yr. A distinct change in Metković active fault slip rates is observed; in the northwestern portion of the fault, the first 30 km slipped at least 1.25 mm/yr, while the slip rate decreases to less than 0.1 mm/yr further to the southeast. The other two active faults containing at least one fault element with an average slip rate exceeding 1 mm/yr are the Mljet (AF19B) and Hvar (AF13B) active faults. The highest average slip rate of 1.43 mm/yr was calculated for the central part of the Mljet active fault. The highest average slip rate of the Hvar active fault is 1.38 mm/yr at its eastern end where the fault bounds the Metković active fault. These results show that the most rapidly deforming parts of the lithosphere are the southeastern coastal and offshore areas.

Generally, fault elements constituting the coastal and internal offshore active faults move at an average speed of 0.2 to 0.7 mm/yr, with the highest slip rates on the southeastern end of the Ravni Kotari (AF08B) and the northwestern part of Imotski active fault (AF12B). However, the external-most thrusts show slip rates that do not exceed 0.2 mm/yr. The only exception is the southeastern end of the Palagruža active fault (AF17C), which has the fastest slip rates among the external offshore fault elements. Similarly low slip rates are found for the strike-slip faults in the northwest of the ED (Zone A). None of the strike-slip fault elements have average slip rates higher than 0.2 mm/yr, and there is a general trend of lower values for the more inland faults.

The Montenegro active fault (AF20B) and the South Adriatic Basin accommodate 65% of the total convergence between the Apulia and Eurasia. The remaining residual velocity with respect to Eurasia is distributed into internal regions where it might be released by other active faults not included in the model. These continuum strain rates predict a prevailing transtensive regime in Albania and transpressive-compressive kinematics for the internal parts of the Dinarides not included in the model (Figure 10). In the central part of the model, active faults release 2 mm/yr of motion that represents 70% of the local Adria - Eurasia compression, leaving 1 mm/yr of horizontal

velocity to be released in more internal regions. Active faults in the northwest of the model (Zone A) absorb only 0.3 - 0.4 mm/yr of the overall 2 mm/yr horizontal velocities, representing 20% of the regional compression. With such low slip rates along these faults, a significant part of the Adria – Eurasia convergence is transmitted into internal areas. Such slip rates are most likely underestimated and reflect the absence of Southern Alps active faults in our model, which would structurally continue the NW-SE striking strike-slip faults of western and southwestern Slovenia.

In Table 3, we report the FEM-modeled slip rate values (maximum, minimum, average) for all active faults used in this study. In the supplementary material (Table 1A), we present a detailed report of the 5th percentile (minimum) values, the median values and the 95th percentile (maximum) values of slip rate for each fault element.

4. DISCUSSION

In the applied method, the variability of FEM slip rates must fulfill two main requirements: consistency with the WSM data and a full exploration of the uncertainties of input parameters (heat flow, crustal thickness, rheology and boundary conditions). The applied $\varepsilon_{m,j} \leq \bar{\varepsilon}_{m,j} - \sigma_{\bar{\varepsilon}}$ criterion satisfied these two requirements. By using this criterion, we simultaneously considered the models that best fit the WSM stress orientations, thus limiting the number of models considered, and we guaranteed a consistent number of models reflecting analysis of input parameter uncertainties. To check if the 596 selected models were appropriate for obtaining stable slip rate results, we performed the calculation of the slip rate fractional change (SRFC) considering all of the 171 fault elements:

$$SRFC = \sum_{m=1}^N \frac{\sum_{i=1}^{171} | \langle sr_{m,i} \rangle - \langle sr_{m-1,i} \rangle |}{171}$$

where m is the number of models considered, sorted for ascending $\varepsilon_{m,j}$ misfit, i is the fault element considered and $sr_{m,f}$ is the slip rate of the i -th segment averaged over N models. The SRFC provides the average variation in slip rates due to the insertion of m -th model in the population of preferred models. For $m = 596$, $SRFC = 0.00028$ mm/yr and $\bar{\varepsilon}_{m,j}$ is 18.23° . These results suggest a good compromise between choosing a low number of models that best agree with WSM data and choosing a sufficient number of models that adequately reflect the input parameter uncertainties (Figure 11).

Due to the paucity and uneven coverage of GPS data, which are mainly concentrated along the coastlines, and a large part of the mesh being located offshore, we decided against scoring the models using geodetic measurements during the processing phase. In the post-processing phase, we checked the consistency of the final horizontal velocities with available GPS measurements [Caporali et al., 2009, Caporali et al., 2011; Devoti et al., 2008; Bennett et al., 2008]. As all the GPS data are in a fixed-Eurasia reference frame, we joined them in a unique GPS dataset. We noted that some of the horizontal velocities along the Dinaric coastline are inconsistent with the tectonic lithospheric horizontal flow and seem to be a response to local phenomena (Figure 12). Some of the GPS benchmarks are located within the mesh, but their horizontal velocities are related to the geodynamics of the Apennines as opposed to compression of the Dinarides. However, we retained all measurements in the GPS dataset to avoid any arbitrary choices. We scored the final horizontal velocities, averaged over the 596 best models, against this GPS dataset following the approach of Liu and Bird [2002]. We obtained a RMS error of 1.40 mm/yr for the final model, indicating good agreement between the modeled and measured horizontal velocities (Figure 12).

Internally based ED faults are the oldest and have become the internal structures of the belt through multiple stages of active compression. They display higher dip angles than younger and more external thrusts and are currently active as strike-slip to oblique strike-slip – reverse faults, while

the coastal and external faults act as thrusts. Such organization of the belt is in accordance with the mechanics and structural evolution of thrust belts [Davis et al., 1983; Dahlen, 1990]. New shallower-dipping faults develop at the edges of the growing convergent structure, while the innermost faults also remain active, possibly with lower effective friction. The paired t-Test shows a statistically significant difference between the models including variable and fixed effective friction, preferring the models with variable $\frac{FA_{(i)}}{FA_{\max}}$. These results agree with other studies showing that the mature active faults appear to be weaker and have lower friction than predicted by theoretical studies [Melosh, 1996; Faulkner and Rutter, 2001; Imber et al., 2001]. Several phenomena can explain mechanical weakness of mature faults and we did not distinguish among the different causes in our models. These results show the important role of fault longevity on fault slip rates.

We found that the Adriatic lithosphere has a high resistance to deformation with respect to the surrounding areas, as shown previously by Tesauro et al. [2009] and Carafa and Barba [2011]. The rheology of Adria plays an important role in the deformation and we think that the strong Adriatic lithosphere is not directly associated with Adria being a rigid, unique and undeformable aseismic block, as is also disproven by seismicity within the Adria microplate [Markušić et al., 2008]. The assumption of an aseismic rigid microplate might neglect the activity of faults with low, but significant, slip rates. These faults are weaker than the surrounding lithosphere and accumulate a variable amount of slip rate. Moreover, considering the Adria microplate as geologically and rheologically homogeneous would neglect important geological features, such as the South Adriatic Basin. This area is characterized by elevated heat flow [Del Ben et al., 1994] and represents a geological structure that has consumed 15 % of the Adria – Eurasia compression (Figure 10).

Our model is not exhaustive and the calculated slip rates could be improved when new data, such as permanent GPS measurements, are available. The low residual anelastic strain rate suggests that introducing additional faults or changing their parameters may have little influence on the obtained slip rates, with the exception of areas where the largest principal strain rate is higher than 10^{-15} s^{-1} (Figure 10). In these places, the obtained slip rates might be underestimated or the model may be missing active faults. The strain rate map (Figure 10) shows that such conditions can be found offshore of northern Montenegro. The FEM results reflect the current understanding of active faulting in the ED due to Adria - Eurasia compression. At the same time, secondary causes, such as the interaction of the ED (AF15C, AF16C, AF17C) with neighboring external Apennine thrusts in the Central Adriatic (Figure 3), can play an important role on ED evolution and consequently on its active fault slip rates. Due to fault interaction and slip rate partitioning among parallel faults in the Central Adriatic, slip rates for the external-most faults of our model can change by adjusting the boundary conditions along the AD edge or by including the external Apennine thrusts in the model. Inserting Southern Alps thrusts could increase slip rates for active faults in Zone A (Figure 3). We address these issues by introducing a composite solution for slip rate.

5. SEISMIC HAZARD IMPLICATIONS

We summarized the current knowledge of ED fault slip rates in Table 3, where we also included the modeling results, available slip rates calculated from GPS data [Benett et al., 2008] and estimated slip rates published by the DISS Working Group [2010]. The latter were estimated from geological [Kralj and Tomljenović, 2009], morphological [Benac et al., 2004; Benac et al., 2008] and geodetic [Caporali et al., 2009] data. We support the usage of available geological and geodetic data for the calculation of fault slip rates and support the use of modeling techniques when data are missing or ambiguous, as suggested by Bird and Kong [1994]. The composite solution includes the range of slip rates obtained by the aforementioned methodologies. Where geological studies or geodetic data

suggest a broader range of slip rates for a given fault than the numerical model estimates, we included these ranges in the composite solution. Future independent and more detailed studies will be needed to explore the lower and upper bounds of slip rates and their variations through geological time. Given the structural setting of faults in the region and the broader geodynamic conditions, we expect future data and models to narrow the slip rate range of the composite solution proposed in this work. The composite solution for active fault slip rates in the ED may be useful also for estimating seismic hazard. In a region where a significant part of the territory is covered by sea and islands, the application of classical seismic hazard calculations based upon macroseismic localization of historical earthquakes tends to locate the hazards inland, leading to an underestimation of seismic hazard for the islands and offshore areas.

The composite solution shows that slip rates for ED active faults generally diminish from southeast to northwest and are lowest for the faults furthest to the northwest and furthest offshore in the central ED. The composite solution also shows that island and offshore faults have slip rates comparable to the coastal and some inland faults. Therefore, these active faults need to be considered as possible sources of future earthquakes and must be included in seismic hazard assessments.

The Montenegro active fault (AF20B) has an average long-term slip rate of 2.01 mm/yr and can be classified as the most active fault in the ED. This active fault also hosted the 1979 Mw 7.1 earthquake, which is the strongest instrumentally recorded earthquake of the ED. The upper edge of the fault is positioned 5 to 20 km from the coast and, as it is a shallowly dipping structure, it poses a threat for significant ground shaking and represents a potential tsunamigenic source. The 1979 earthquake caused severe damage throughout Montenegro and northern coastal and inland Albania [Pichard, 1979; Aničić et al., 1980], with peak ground accelerations of 0.49 g [Aničić et al., 1980]. Soloviev et al. [2000] reports recorded tsunami waves at tide gauges in Montenegro and the

southern Croatian coast caused by the earthquake. Maximum tsunami wave heights of 0.5 m for the central and southern Montenegro coast were modeled as an effect of fault displacement along the Montenegro fault [Tiberti et al., 2008].

The active Mljet (AF19B), Hvar (AF13B), Vis-Korčula (AF14B) and Metković (AF18B) faults located in the central and southeastern ED show the highest slip rate variability. This variability includes the findings of Bennett et al. [2008], who calculated a loading rate of 4.2–5.0 mm/yr on a single buried fault plane dipping 8°–15° with an assumed strike 283°. Our FEM modeling results never exceed 3.50 mm/yr for the maximum (95th percentile value) slip rate value for fault elements located in the area investigated by Bennett et al. [2008], whereas geological indicators give a maximum value of 1.0 mm/yr (see Table 3). The structural setting of various parallel faults typical for the ED would suggest that such structures are capable of causing deformation simultaneously. Therefore, the cumulative slip rate would be partitioned among the faults, resulting in lower slip rates than if all displacement were along one fault. Such a model is a more realistic situation for the ED. Therefore, future, more precise studies on geological and structural conditions will refine the composite slip rate values. To not exclude the available slip rates from the composite slip rate estimates a priori, we set the upper limit of the Mljet, Hvar, Vis-Korčula and Metković Faults according to the lower-bound slip rates obtained by Bennett et al. [2008].

The tectonic activity in Zone C seems to interact with active diapirism, as observed from the seismic profiles published by Geletti et al. [2008] and evidenced by the 1988 Palagruža [Markušić et al., 1990] and 2003 Jabuka [Herak et al., 2005] seismic sequences. A similar geologic setting of coexisting active faults, active diapirism and evaporitic layers is also found for the Montenegro (AF20B) and the southern part of the Mljet (AF19B) active faults, where the evaporitic body is closer to the coast and continues further south into Albania and Greece [Velaj, 2002]. The available

information on slip rates does not consider the possible influence of active diapirism on long-term slip rates and we cannot exclude that local diapirism increases slip rates.

The fastest-moving faults approach the critical stress needed for fault activation or reactivation sooner than slow-moving faults and are more directly associated with causing large earthquakes. For example, the Montenegro active (AF20B) is associated with the 1979 M_w 7.1 earthquake. Conversely, the ED also offers examples of the opposite: despite the Tolmin-Idrija active fault (AF03A) being a slow-moving fault, it was the source of the destructive 1511, M 6.8 earthquake. This is an important reminder that slow-moving faults need to be given attention in seismic hazard studies, particularly because faults in less seismically active areas tend to be studied less. Slow-moving faults cause less frequent, but not necessarily weaker, earthquakes and tend to produce smaller morphological imprints. Therefore, these faults are more difficult to study, are usually less well known and are sources of high risk.

6. CONCLUSIONS

Thin-shell models incorporating active faults, lithospheric and rheological characteristics, laterally varying thermal structure and appropriate geodynamic boundary conditions have been used to simulate the regional neotectonics of the External Dinarides and to determine active fault slip rates. This study is the first dynamic model of the area.

The models indicate highest slip rates for active faults in the southeastern External Dinarides and their gradual decrease to the northwest, reaching minimum values for the northwesternmost faults. Low slip rates are also characteristic for external offshore faults. The mechanical properties of the faults and their geological evolution have an important role on the release of slip and must be included in dynamic models.

We propose slip rates for active faults in the External Dinarides based upon the results of our models and taking into consideration other available geological and geodetic information. These slip rates allow improvements in long-term seismic hazard estimates, as they also consider physical properties and the geodynamic background of the External Dinarides.

ACKNOWLEDGMENTS

This research was supported by the EU-EP7-funded project Seismic Hazard Harmonization in Europe SHARE (Grant no. 226967) and partially supported by DPC-INGV 2008-2010 S1 project. The authors would like to acknowledge the insightful suggestions on the early version of the manuscript by S. Barba and R. Basili and to acknowledge S. Barba for his further suggestions and comments. The authors would also like to acknowledge P. Bird for the open source availability of SHELLS. Reviews by F. Calamita, an anonymous reviewer and the Associate Editor noted shortcomings of the manuscript, thus improving its final version.

REFERENCE LIST

Albini, P. (2004), A survey of the past earthquakes in the Eastern Adriatic (14th to early 19th century), *Annals of Geophysics*, 47 (2/3), 675-703.

Amante, C. and B. W. Eakins (2009), ETOPO1 1 Arc-Minute Global Relief Model: Procedures, Data Sources and Analysis, NOAA Technical Memorandum NESDIS NGDC-24, 19 pp., Available at <http://www.ngdc.noaa.gov/mgg/global/global.html>.

Anderson, H., and J. Jackson (1987), Active tectonics of the Adriatic region, *Geophys. J. R. Astron. Soc.*, 91, 937–983.

Aničić, D., G. Berz, D. Boore, J. Bouwkamp, U. Hakenbeck, R. McGuire, J. Sims, and G. Wieczorek (1980), Reconnaissance report: Montenegro, Yugoslavia earthquake April 15, 1979, *Earthquake Engineering Research Institute Reconnaissance Report*, p. 90.

Advanced National Seismic System (ANSS) Composite Earthquake Catalog, Northern California Earthquake Data Center, available at <http://quake.geo.berkeley.edu/cnss/>.

Argnani, A. (1998), Structural elements of the Adriatic foreland and their relationships with the front of the Apennine fold-and thrust belt, *Mem. Soc. Geol. Ital.*, 52, 647–654.

Bajc, J., A. Aoudia, A. Saraò, and P. Suhadolc (2001), The 1998 Bovec Krn Mountain (Slovenia) Earthquake Sequence. *Geophys. Res. Lett.*, 28(9), 1839–1842, doi:10.1029/2000GL011973.

Barba, S., M. M. C. Carafa, and E. Boschi (2008), Experimental evidence for mantle drag in the Mediterranean, *Geophys. Res. Lett.*, 35, L06302, doi:10.1029/2008GL033281.

Basili, R., G. Valensise, P. Vannoli, P. Burrato, U. Fracassi, S. Mariano, M.M. Tiberti, and E. Boschi (2008), The Database of Individual Seismogenic Sources (DISS), version 3: summarizing 20 years of research on Italy's earthquake geology, *Tectonophysics*, 10.1016/j.tecto.2007.04.014.

Benac, C., M. Juračić, and T. Bakran-Petricioli (2004), Submerged tidal notches in the Rijeka Bay NE Adriatic Sea: indicators of relative sea-level change and of recent tectonic movements, *Mar. Geol.*, 212, 21-33.

Benac, C., M. Juračić, and I. Blašković (2008), Tidal notches in Vinodol Channel and Bakar Bay, NE Adriatic Sea: Indicators of recent tectonics, *Mar. Geol.*, 248, 151-160.

Benetatos, C. and A. Kiratzi (2006), Finite-fault slip models for the 15 April 1979 (Mw 7.1) Montenegro earthquake and its strongest aftershock of 24 May 1979 (Mw 6.2), *Tectonophysics*, 421, 129-143, 10.1016/j.tecto.2006.04.009.

Bennett, R. A., S. Hreinsdóttir, G. Buble, T. Bašić, Ž. Bačić, M. Marjanović, G. Casale, A. Gendaszek, and D. Cowan (2008), Eocene to present subduction of southern Adria mantle lithosphere beneath the Dinarides, *Geology*, 36(1), 3 - 6.

Bird, P. (1989), New finite element techniques for modeling deformation histories of continents with stratified temperature-dependent rheology, *J. Geophys. Res.*, 94(B4), 3967–3990, doi:10.1029/JB094iB04p03967.

Bird, P. (1996), Computer simulations of Alaskan neotectonics, *Tectonics*, 15(2), 225-236.

Bird, P. (1999), Thin-plate and thin-shell finite element programs for forward dynamic modeling of plate deformation and faulting, *Comput. Geosci.*, 25(4), 383-394.

Bird, P. and X. Kong (1994), Computer simulations of California tectonics confirm very low strength of major faults, *Geol. Soc. Am. Bull.*, 106(2), 159-174.

Bird, P., Z. Liu, and W. K. Rucker (2008), Stresses that drive the plates from below: Definitions, computational path, model optimization, and error analysis. *J. Geophys. Res.*, 113, B11406, doi:10.1029/2007JB005460.

Boccaletti, M., F. Calamita, and M.G. Viandante (2005), La Neo-Catena litosferica appenninica nata a partire dal pliocene inferiore come espressione della convergenza Africa– Europa, *Boll. Soc. Geol. Ital.*, 124, 87–105.

Brandmayr, E., R. Blagoeva Raykova, M. Zuri, F. Romanelli, C. Doglioni, and G. F. Panza (2010), The lithosphere in Italy: structure and seismicity. *Journal of the Virtual Explorer*, 36 (1), doi:10.3809/jvirtex.2010.00224.

Burchfiel, B. C., R. W. King, A. Todosov, V. Kotzev, N. Durmurdzanov, T. Serafimovski, and B. Nurce (2006), GPS results for Macedonia and its importance for the tectonics of the Southern Balkan extensional regime, *Tectonophysics*, 413 (3-4), 239-248, DOI:10.1016/j.tecto.2005.10.046.

Caporali, A. (2007), Geophysical characterization of the main seismogenic structures, in *Final Reports of the Project: Assessing the Seismogenic Potential and the Probability of Strong Earthquakes in Italy*, edited by D. Slejko and G. Valensise, pp. 25 – 42, INGV, Rome. (available at <http://hdl.handle.net/2122/3090>).

Caporali, A., C. Aichhorn, M. Barlik, M. Becker, I. Fejes, L. Gerhatova, D. Ghitau, G. Grenerczy, J. Hefty, S. Krauss, D. Medak, G. Milev, M. Mojzes, M. Mulić, A. Nardo, P. Pesec, T. Rus, J. Simek, J. Sledzinski, M. Solarić, G. Stangl, and B. Stopar (2009), Surface kinematics in the Alpine-Carpathian-Dinaric and Balkan region inferred from a new multi-network GPS combination solution, *Tectonophysics*, 474 (1-2), 295-321, 10.1016/j.tecto.2009.04.035.

Caporali, A., S. Barba, M. M. C. Carafa, R. Devoti, G. Pietrantonio, and F. Riguzzi (2011), Static stress drop as determined from geodetic strain rates and statistical seismicity, *J. Geophys. Res.*, 116, B02410, doi:10.1029/2010JB007671.

Carafa, M. M. C. and S. Barba (2011), Determining rheology from deformation data: The case of central Italy, *Tectonics*, 30, TC2003, doi:10.1029/2010TC002680.

Cloetingh, S., P.A. Ziegler, F. Beekman, P.A.M. Andriessen, L. Matenco, G. Bada, D. Garcia-Castellanos, N. Hardebol, P. Dezes, and D. Sokoutis (2005), Lithospheric memory, state of stress and rheology: neotectonic controls on Europe's intraplate continental topography, *Quat. Sci. Rev.*, 24 (3-4), 241-304 pp, doi: 10.1016/j.quascirev.2004.06.015.

Collettini, C., and R. E. Holdsworth (2004), Fault zone weakening and character of slip along low-angle normal faults: Insights from the Zuccale Fault, Isle of Elba, Italy, *J. Geol. Soc.*, 161, 1039–1051, doi:10.1144/0016-764903-179.

Dahlen, F. A. (1990), Critical taper model of fold-and-thrust belts and accretionary wedges, *Earth Planet. Sci. Lett.*, 19, 55-99.

Davis, D., J. Suppe, and F. A. Dahlen (1983), Mechanics of fold-and-thrust belts and accretionary wedges, *J. Geophys. Res.*, *88*, 1153-1172.

Del Ben, A., I. Finetti, F. Mongelli and G. Zito (1994), Seismic and heat flow study of the southern Adriatic Basin, *Boll. Geofis. Teor. Appl.*, *36* (141-144), 29-44.

Del Ben, A., R. Geletti and A. Mocnik (2010), Relation between recent tectonics and inherited Mesozoic structures of the central-southern Adria plate, *Boll. Geofis. Teor. Appl.*, *51* (2-3), 99-115.

Della Vedova, B., S. Bellani, G. Pellis, and P. Squarci (2001), Deep temperatures and surface heat flow distribution. In: *Anatomy of an orogen, The Apennines and adjacent Mediterranean basins*, edited by Vai G.B. and I.P. Martini, Kluwer Academy Publishers, Dordrecht, The Netherlands.

Devoti, R., F. Riguzzi, M. Cuffaro and C. Doglioni (2008), New GPS constraints on the kinematics of the Apennines subduction, *Earth Planet. Sci. Lett.*, *273* (1-2), 163-174, DOI: 10.1016/j.epsl.2008.06.031.

Dimanov, A. and G. Dresen (2005), Rheology of synthetic anorthite-diopside aggregates: Implications for ductile shear zones, *J. Geophys. Res.*, *110*, B7, doi:10.1029/2004JB003431.

DISS Working Group (2009), Database of Individual Seismogenic Sources (DISS), Version 3.1.0: A compilation of potential sources for earthquakes larger than M 5.5 in Italy and surrounding areas. <http://diss.rm.ingv.it/diss/>, © INGV 2009 - Istituto Nazionale di Geofisica e Vulcanologia - All rights reserved.

DISS Working Group (2010), Database of Individual Seismogenic Sources (DISS), Version 3.1.1: A compilation of potential sources for earthquakes larger than M 5.5 in Italy and surrounding areas. <http://diss.rm.ingv.it/diss/>, © INGV 2010 - Istituto Nazionale di Geofisica e Vulcanologia - All rights reserved.

Drobne, K. and R. Pavlovec (1991), Paleocene and Eocene Beds in Slovenia and Istria, in: *Introduction to the Paleogene of SW Slovenia and Istria Field Trip Guidebook, Second meeting IGCP project 286*, edited by Drobne, K. and R. Pavlovec, pp 7–17, Ljubljana.

Faccenna, C. and T. W. Becker (2010), Shaping mobile belts by small scale convection, *Nature*, 465, 602–605, doi:10.1038/nature0906.

Fantoni R. and R. Franciosi (2010), Tectono-sedimentary setting of the Po Plain and Adriatic Foreland, *Rendiconti Lincei*, 21 (1), S197–S209, doi 10.1007/s12210-010-0102-4.

Faulkner D. R. and E. H. Rutter (2001), Can the maintenance of overpressured fluids in large strike–slip fault zones explain their apparent weakness?, *Geology*, 29, 503–506.

Finetti, I. R. and A. Del Ben (2005), Crustal tectono- stratigraphic setting of the Adriatic Sea from new CROP seismic data. In: *CROP Project: Deep Seismic Exploration of the Central Mediterranean and Italy*, edited. by I.R. Finetti, Elsevier, Amsterdam.

Fowler, S.W., J.-C. Miquel, and J. La Rosa (1998), 210Pb Dating of Sediments from the Central and Northern Adriatic Sea: Deposition and Preservation of Sedimentary Organic Carbon, Ecosystems Research Report, The Adriatic Sea, EU/Environment Series, Brussels EEC Conference on Physical and Biogeochemical Processes of the Adriatic Sea, Ancona, Italy, April 23–27, 1996.

Gambini, R., R. Thomas and S. Morandi (1997), Inversion Tectonics on the Central Adriatic Sea. *Abstracts FIST Geitalia*, 2, 170-171.

Geist, E. L. and D. J. Andrews (2000), Slip rates on San Francisco Bay area faults from anelastic deformation of the continental lithosphere, *J. Geophys. Res.*, 105, 25,543 – 25,552.

Geletti, R., A. Del Ben, M. Busetti, R. Ramella and V. Volpi (2008), Gas seeps linked to salt structures in the Central Adriatic Sea, *Basin Res.*, 20, 473–487, doi: 10.1111/j.1365-2117.2008.00373.x.

Grad, M., Tiira, T. and ESC Working Group (2009), The Moho depth map of the European Plate, *Geophysical Journal International*, 176, 279–292. doi: 10.1111/j.1365-246X.2008.03919.x.

Grandić, S., E. Boromisa-Balaš, M. Šušterčić and S. Kolbah (1999), Hydrocarbon possibilities in the Eastern Adriatic Slope zone of Croatian offshore area, *Nafta (Zagreb, Croatia)*, 50 (2), 51–73.

Grandić, S. and Ž. Markulin (2000), Triassic synrift euxinic basins as a factor of exploration risk in the Croatian offshore area, in proceedings of *International Symposium of Petroleum Geology, Nafta* Sp. Issue, pp. 41–50, Zagreb.

Grandić, S., I. Kratković, and S. Kolbah (2007), Review of the hydrocarbon layers in the Croatian offshore and Periadriatic areas, *Nafta (Zagreb, Croatia)*, 58 (3), 146-158.

Grenerczy, G., G. Sella, S. Stein and A. Kenyeres (2005), Tectonic implications of the GPS velocity field in the northern Adriatic region, *Geophys. Res. Lett.*, 32, L16311, 10.1029/2005GL022947.

Heidbach, O., J. Reinecker, M. Tingay, B. Müller, B. Sperner, K. Fuchs, and F. Wenzel (2007), Plate boundary forces are not enough: Second- and third-order stress patterns highlighted in the World Stress Map database, *Tectonics*, 26, TC6014, doi:10.1029/2007TC002133.

Heidbach, O., M. Tingay, A. Barth, J. Reinecker, D. Kurfeß, and Müller, B. (2008), The World Stress Map database release 2008 doi:10.1594/GFZ.WSM.Rel2008.

Herak D., M. Herak, E. Prelogović, S. Markusić, and Ž. Markulin (2005), Jabuka island (Central Adriatic Sea) earthquakes of 2003, *Tectonophysics*, 398, 167-180, DOI: 10.1016/j.tecto.2005.01.007.

Herak, M., D. Herak, and S. Markušić (1995), Fault plane solutions for earthquakes (1956-1995) in Croatia and neighbouring regions, *Geofizika*, 12, 43-56.

Herak, M., D. Herak, and S. Markušić (1996), Revision of the earthquake catalogue and seismicity of Croatia, 1908-1992, *Terra Nova*, 8, 86-94.

Howe, T. C. and P. Bird (2010), Exploratory models of long-term crustal flow and resulting seismicity in the Alpine-Aegean orogen, *Tectonics*, 29, TC4023, doi:10.1029/2009TC002565.

Imber, J., R. E. Holdsworth, C. A. Butler, and R. A. Strachan (2001), A reappraisal of the Sibson-Scholz fault zone model: The nature of the frictional to viscous (“brittle-ductile”) transition along a long-lived, crustal-scale fault, Outer Hebrides, Scotland, *Tectonics*, 20, 601–624, doi:10.1029/2000TC001250.

Imber, J., R. E. Holdsworth, S. A. F. Smith, S. P. Jefferies and C. Collettini (2008), Frictional-viscous flow, seismicity and the geology of weak faults: a review and future directions, in *The Internal Structure of Fault Zones: Implications for Mechanical and Fluid-Flow Properties*, edited by Wibberley, C. A. J., W. Kurz, J. Imber, R. E. Holdsworth, C. Collettini, pp. 151–173, Geological Society Special Publications, London.

Ismail-Zadeh, A., A. Aoudia, and G. F. Panza (2010), Three-dimensional numerical modeling of contemporary mantle flow and tectonic stress beneath the Central Mediterranean, *Tectonophysics*, 482 (1-4), 226-236, DOI: 10.1016/j.tecto.2009.07.013.

Ivančić, I., D. Herak, S. Markušić, I. Sović, and M. Herak (2006), Seismicity of Croatia in the period 2002-2005, *Geofizika*, 23(2), 87-103.

Karato, S.I. (1984), Grain-size distribution and rheology of the upper mantle, *Tectonophysics*, 104 (1-2), 155–176, doi: 10.1016/0040-1951(84)90108-2.

Kastelic, V., M. Vrabc, D. Cunningham, and A. Gosar (2008), Neo-Alpine structural evolution and present-day tectonic activity of the eastern Southern Alps: The case of the Ravne Fault, NW Slovenia, *J. Struct. Geol.*, 30 (8), 963-975, DOI:10.1016/j.jsg.2008.03.009.

Korbar, T. (2009), Orogenic evolution of the External Dinarides in the NE Adriatic region: a model constrained by tectonostratigraphy of Upper Cretaceous to Paleogene carbonates, *Earth-Sci. Rev.*, 96 (4), 296-312, doi: 10.1016/j.earscirev.2009.07.004.

Koyi, H., A. K. Hessami, and A. Teixell (2000), Epicenter distribution and magnitude of earthquakes in fold and thrust belts: Insights from Sandbox Models, *Geophys. Res. Lett.*, 27(2), 273–276, doi:10.1029/1999GL010833.

Kralj, K. and B. Tomljenović (2009), An overview on structures and structural styles in the Adriatic Offshore, Croatia, *Rendiconti online Società Geologica Italiana*, 9, 41-42.

Kuk, V., E. Prelogović, and I. Dragičević (2000), Seismotectonically active zones in the Dinarides, *Geologia Croatica*, 53 (2), 295-303.

Lankreijer, A., V. Mocanu, and S. Cloetingh (1997), Lateral variations in lithosphere strength in the Romanian Carpathians: constraints on basin evolution, *Tectonophysics*, 272, 269–290.

Liu, Z. and P. Bird (2002), Finite element modeling of neotectonics in New Zealand, *J. Geophys. Res.*, 107(B12), 2328, doi:10.1029/2001JB001075.

Marjanac, T., D. Babac, J. Benić, J., V. Čosović, K. Drobne, L. Marjanac, R. Pavlovec, and Z. Velimirović (1998), Eocene carbonate sediments and sea-level changes on the NE part of Adriatic carbonate platform (Island of Hvar and Pelješac peninsula, Croatia), in *Paleogene shallow benthos of the Tethys*, 2, *Dela-Opera SAZU* 4, 32 (2), edited by Hottinger, L. and Drobne, K., pp. 203–242.

Markušić S. (2008), Seismicity of Croatia. In: E.S. Husebye (ed.), Earthquake Monitoring and Seismic Hazard Mitigation 81 in Balkan Countries, *NATO Science Series*, 81(II), 81-98, doi: 10.1007/978-1-4020-6815-7_5.

Markušić, S., I. Sović, and D. Herak, (1990), Seismicity of Croatia and the surrounding areas in 1988, *Geofizika*, 7, 121–134.

Melosh, H. J. (1996), Dynamical weakening of faults by acoustic fluidization, *Nature*, 379, 601–606, doi:10.1038/379601a0.

Milivojević, M. (1993), Geothermal model of Earth's crust and lithosphere for the territory of Yugoslavia: some tectonic implications. *Study geoph. et geod.*, 37, 265-278.

Papazachos, B.C., Comninakis, P.E., Scordilis, E.M., Karakaisis, G.F., and C.B. Papazachos (2009), A catalogue of earthquakes in the Mediterranean and surrounding area for the period 1901 - Sep2009, Publ. Geophys. Laboratory, University of Thessaloniki, Thessaloniki.

Pichard, P. (1979), Restoration of the cultural heritage of Montenegro after the earthquake of 15 April 1979, UNESCO Restricted Technical Report RP/1979-80/4/7.6/05. 40 pp.

Ribarič, V. (1979), The Idrija earthquake of March 26, 1511 – a reconstruction of some seismological parameters, *Tectonophysics*, 53(3-4), 315-324.

Ribarič, V. (1982), Seizmičnost Slovenije, Katalog potresov (792 n.e.-1981), 649 pp., Seizmološki zavod SR Slovenije, Ljubljana.

Scholz C.H. (1998), Earthquakes and friction laws, *Nature*, 391, p. 37–42, doi:10.1038/34097.

Scisciani, V. and F. Calamita, (2009), Active intraplate deformation within Adria: Examples from the Adriatic region, *Tectonophysics*, 476 (1–2), 57-72 pp, 10.1016/j.tecto.2008.10.030.

Scrocca, D. (2006) Thrust front segmentation induced by differential slab retreat in the Apennines (Italy), *Terra Nova*, 18, 154-161 , doi: 10.1111/j.1365-3121.2006.00675.x.

Soloviev, S. L., O. N. Solovieva, C. N. Go, K. S. Kim, and N. A. Shchetnikov (2000), Tsunamis in the Mediterranean Sea 2000 B.C.–2000 A.D., in *Advances in Natural and Technological Hazards Research Series*, 260 pp, Kluwer Academic Publishers, Hingham, Massachusetts.

Stucchi, M., R. Camassi, A. Rovida, M. Locati, E. Ercolani, C. Meletti, P. Migliavacca, F. Bernardini, and R. Azzaro (2007), DBMI04, il database delle osservazioni macrosismiche dei terremoti italiani utilizzate per la compilazione del catalogo parametrico CPTI04 <http://emidius.mi.ingv.it/DBMI04/>. Quaderni di Geofisica, INGV, 49, 38.

Suppe, J., Huang, Mong-Han, and Carena, S., 2009, Mechanics of thrust belts and the weak fault/strong-crust problem, *Trabajos de Geologia*, 29, 51-55.

Tari, V. (2002), Evolution of the Northern and Western Dinarides: A Tectonostratigraphic Approach, *EGU Special Publication Series*, 1 , 223–236.

Tari-Kovačić, V. (1998), Geodynamics of the Middle Adriatic offshore area, Croatia, based on stratigraphic and seismic analysis of Paleogene beds, *Acta Geol. Hung.*, 41 (3), 313–326.

Tari-Kovačić, V., K. Kalac, D. Lučić, and J. Benić (1998), Stratigraphic analysis of Paleogene beds in some off-shore wells (Central Adriatic area, Croatia), in *Paleogene shallow benthos of the Tethys*, 2, *Dela-Opera SAZU* 4, 32 (2), edited by Hottinger, L. and Drobne, K., pp. 203–242.

Tesauro, M., M.K. Kaban, and S.A.P.L. Cloetingh (2009), How rigid is Europe's lithosphere? *Geophysical Research Letters*, 36, L16303, doi:10.1029/2009GL039229.

Tiberti, M. M., S. Lorito, R. Basili, V. Kastelic, A. Piatanesi, and G. Valensise (2008), Scenarios of earthquake-generated tsunamis in the Adriatic Sea, *Pure Appl. Geophys.*, 165 (11-12), 2117-2142, DOI: 10.1007/s00024-008-0417-6.

Ustaszewski, K., S. M. Schmid, B. Fügenschuh, M. Tischler, E. Kissling and W. Spakman (2008), A map.view restoration of the Alpine Carpathian Dinaridic system for the Early Miocene, *Swiss J. Geosci.*, 101 (1), 273-294, doi:10.1007/s00015-008-1288-7.

Velaj, T. (2002), Evaporites in Albania and their impact on the thrusting processes, *Carbonates Evaporites*, 17(1), 68-78 .

Watts, A. B. (2001). *Isostasy and Flexure of the Lithosphere*, 458 pp., Cambridge University Press, Cambridge.

Zoback, M. L. (1992), First- and second-order patterns of stress in the lithosphere: The World Stress Map project, *J. Geophys. Res.*, 97(B8), 11,703–11,728.

Figure Captions:

Figure 1

The regional geodynamic setting. Multicolor lines show the SHmax orientations for different kinematic regimes (Heidbach et al., 2008). Tectonic regime identifiers: NF, normal fault; NS, normal-oblique; SS, strike-slip; TS, thrust-oblique; TF, thrust; U, unknown tectonic regime. Seismicity (1976–2010) is shown as gray circles [ANSS Catalog]. The four largest earthquakes [Stucchi et al., 2007; Papazachos et al., 2009] are depicted by red circles. The inset shows the geographic location of the study area (black rectangle) on a larger scale. The dashed gray line locates the profiles showed in Figure 2.

Figure 2

Schematic profiles across the study area. a) Simplified upper crustal geological profile. Structural and stratigraphic units are taken from Grandić and Markulin [2000], Tari [2002], Herak et al., [2005], Scisciani and Calamita [2009] and Fantoni and Franciosi [2010]. b) Schematic lithospheric profile taken from Brandmayr et al. [2010]. The study area is shown within the light red rectangle, while the gray rectangle covers the unmodeled area. Note the different depth ranges of profiles a and b.

Figure 3

Characteristics of the modeled active faults. The upper edges of faults are represented as red lines. Stereographic projections of the minimum and maximum values of the geometrical (strike and dip) and kinematic (rake) characteristics of each active fault are shown. Zones containing geologically and structurally homogeneous groups of faults are shown in dotted blue polygons. Dark gray lines indicate neighboring faults of the DISS [DISS Working Group, 2010] that are seismically active, but not included in our model. Geographic projection with WGS84 datum.

Figure 4

The finite element grid used in this study. Thin gray lines represent continuum element edges, thick red lines represent the upper edges of the modeled fault elements, and orange lines represent active faults that are part of the DISS [DISS Working Group, 2010], but were not modeled in this study. The different color lines and arrows at the edge of the grid represent the applied boundary conditions (more details in the text), while the dashed dark green line represents the inner boundary conditions taken from Barba et al. [2008].

Figure 5

Plots of $\frac{FA_{(i)}}{FA_{\max}}$ for the active ED faults organized into three zones (see Figure 2) versus time for an analogue model with a low-friction decollement [modified after Koyi et al, 2000]. The upper horizontal axis represents geological time in millions of years (MA). Horizontal gray bars are located at the beginning of fault activity in each of the zones. The lower horizontal axis represents the experimental time expressed in seconds. The vertical bar indicates the present $\frac{FA_{(i)}}{FA_{\max}}$ and is set to 0.85 for faults in Zone A, 0.70 for faults in Zone B and 0.20 for faults in Zone C. The experimental time axis intersects the $\frac{FA_{(i)}}{FA_{\max}}$ axis at a value of 0.10.

Figure 6

Model results. Histograms showing: (a) SHmax misfit of the 6912 models (Group V); (b) Lithosphere Upper Mantle Rheology (RMAN) of the 596 best models; (c) Crustal rheology (RCRU) of the 596 best models. See the text for a more detailed description.

Figure 7

Average horizontal surface velocity field obtained over the 596 best models. Long-term slip rates in mm/yr are shown along fault traces.

Figure 8

Average stress field obtained over the 596 best models. The SHmax directions for the study area are shown as bold gray lines. The SHmax directions, tectonic regime and uncertainty ranges of the World Stress Map data [Heidbach et al., 2008] are shown as multicolor lines. Tectonic regime identifiers: NF, normal fault; NS, normal-strike; SS, strike-slip; TS, thrust-strike; TF, thrust; U, unknown tectonic regime. The image to the left shows the northern sector and the image to the right shows the southern sector.

Figure 9

Average long-term fault slip rates obtained over the 596 best models. The width of each colored band is proportional to long-term slip rate. The blue and green bands represent thrust and dextral strike-slip faulting, respectively. The numerical values plotted above the fault traces are the average slip rates for each fault element. Each active fault is coded with its corresponding alphanumeric

value. To insure image clarity, selected values for each fault element are plotted. The entire dataset of slip rates is available in the auxiliary material.

Figure 10

Average continuum strain rates, expressed as micro-fault orientations, obtained over the 596 best models. Dumbbell symbols show conjugate thrust faulting; X symbols show conjugate strike-slip faulting; blank rectangles show conjugate normal faulting. The fault symbols are plotted with their area proportional to their strain rate.

Figure 11

Slip rate stability test shown as the fractional change of fault slip rates with respect to the increasing number of the considered models, sorted with respect to $\bar{\epsilon}_{m,v}$. The vertical black line represents the 596 models considered for the final calculations.

Figure 12

Computed fault-locked horizontal velocities (red arrows) compared to GPS measurements (green arrows) from Caporali et al. [2009], Caporali et al. [2011], Devoti et al. [2008], Bennett et al. [2008] and Howe and Bird [2010]. GPS velocities are shown with their 90% confidence ellipses.

Table Captions

Table 1

Parameters of the modeled active faults.

Table 2

Power-law creep rheologies for the crust and mantle with corresponding references for the approximate laboratory power-law creep rheologies. RMAN3 and RMAN4 are introduced in this study and fill the gap between the RMAN2 and RMAN5 rheologies.

Table 3

Slip rates of the active faults in the External Dinarides.

Active Fault Code	Active Fault Name	Zone Name	Min Depth (km)	Max Depth (km)	Strike Min	Strike Max	Strike Average
AF01A	Bovec-Tolminka Springs	A	1	10	300	320	310
AF02A	Polovnik	A	1	7	275	310	292.5
AF03A	Tolmin-Idrija	A	1	14	290	330	310
AF04A	Cividale-Nova Gorica	A	1	9	300	335	317.5
AF05A	Branik-Ilirska Bistrica	A	1	12	300	325	312.5
AF06B	Vinodol - Rijeka	B	1	15	310	325	317.5
AF07B	Velebit	B	1	18	270	340	305
AF08B	Ravni Kotari	B	2	20	300	330	315
AF09B	Novigrad	B	1	10	300	340	320
AF10B	Zadar	B	2	15	280	310	295
AF11B	Dugi Otok	B	2	18	280	330	305
AF12B	Imotski	B	2	20	290	320	305
AF13B	Hvar	B	2	15	260	310	285
AF14B	Vis-Korčula	B	2	15	270	320	295
AF15C	Eastern Adriatic offshore	C	2	12	270	310	290
AF16C	Jana-1	C	2	12	275	350	312.5
AF17C	Palagruža	C	2	12	275	350	312.5
AF18B	Metković	B	2	18	290	320	305
AF19B	Mljet	B	1	15	280	330	305
AF20B	Montenegro offshore	B	3	15	290	330	310

Dip Min	Dip Max	Dip Average	Rake Min	Rake Max	Rake Average
70	85	77.5	160	180	170
45	70	57.5	120	145	132.5
70	85	77.5	160	180	170
40	85	62.5	120	180	150
70	85	77.5	160	180	170
45	60	52.5	100	140	120
45	70	57.5	80	140	110
45	65	55	95	130	112.5
45	70	57.5	95	130	112.5
45	70	57.5	95	130	112.5
30	55	42.5	90	120	105
50	70	60	95	130	112.5
40	70	55	20	70	45
40	70	55	20	70	45
35	60	47.5	70	100	85
35	50	42.5	70	100	85
35	50	42.5	70	100	85
45	65	55	95	120	107.5
30	45	37.5	70	110	90
10	40	25	60	100	80

	NAME	APPROXIMATE LABORATORY POWER LAW CREEP RHEOLOGY
CRUST	RCRU1	Westerly granite
	RCRU2	Quartzite wet
	RCRU3	Quartz diorite
	RCRU4	Quartzite dry
	RCRU5	Anorthosite
	RCRU6	Diabase dry
MANTLE	RMAN1	Dunite wet
	RMAN2	Olivine dry
	RMAN3	This work
	RMAN4	This work
	RMAN5	Enstatite
	RMAN6	Clinopyroxene
	RMAN7	Olivine
	RMAN8	Diopside

REFERENCE

Hansen and Carter, 1983

Hansen, 1982

Hansen, 1982

Brace and Koldstedt, 1980

Shelton and Tullis, 1981

Mackwell et al. , 1998

Chopra and Patterson, 1981

Karato and Jung, 2003

This work

This work

Lawlis 1998

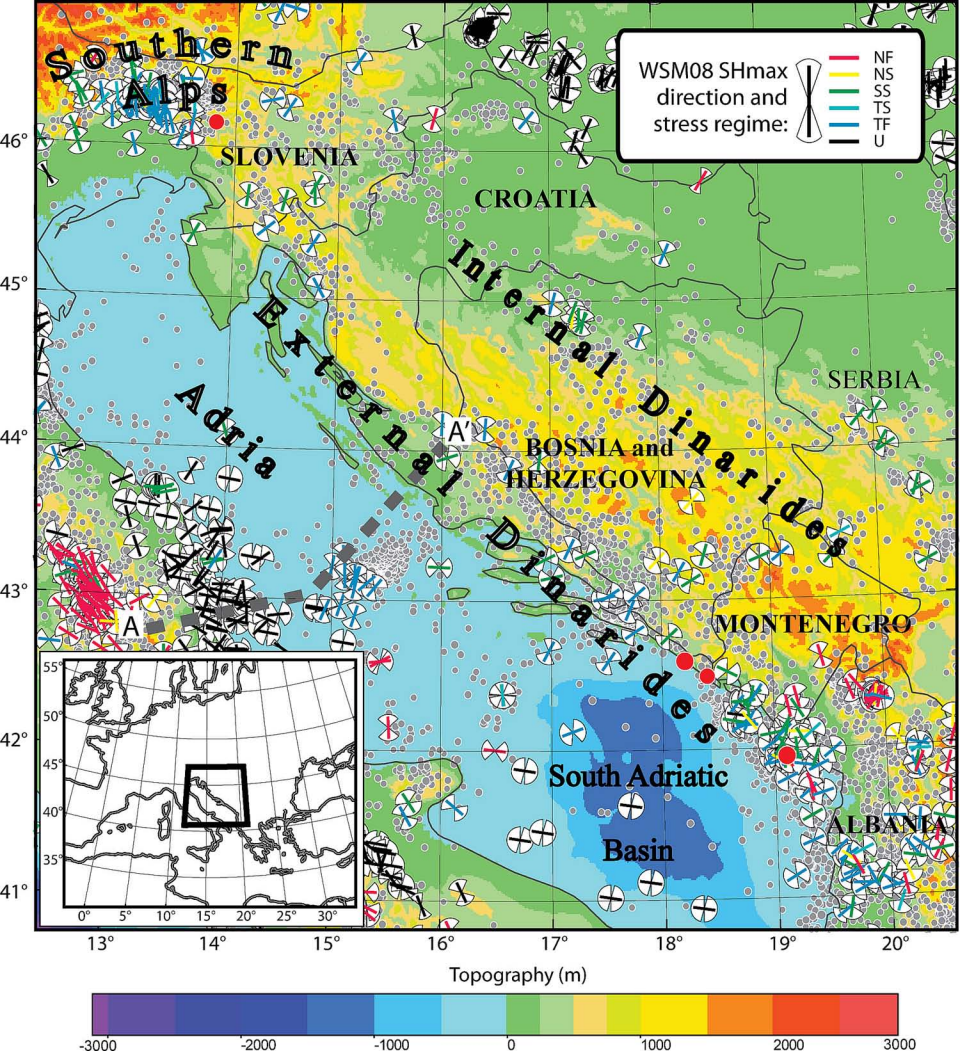
Chen et al., 2006

Hirth and Kohlstedt, 2003

Dimanov and Dresen, 2005

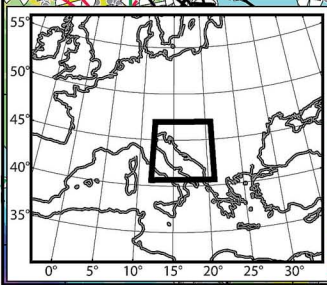
Active Fault Code	Active Fault Name	Zone Name	Slip rate (m		
			Estimated [DISS WG, 2010]	Modeled from Geodetic data [Bennett et al., 2008]	
					Min
AF01A	Polovnik	A	0.10 - 1.00	/	0.02
AF02A	Bovec-Tolminka Springs	A	0.10 - 0.50	/	0.03
AF03A	Tolmin-Idrija	A	0.10 - 0.50	/	0.06
AF04A	Cividale-Nova Gorica	A	0.10 - 0.50	/	0.05
AF05A	Branik-Ilirska Bistrica	A	0.10 - 0.50	/	0.08
AF06B	Vinodol - Rijeka	B	0.20 - 0.50	/	0.08
AF07B	Velebit	B	0.10 - 0.50	/	0.13
AF08B	Ravni Kotari	B	0.10 - 1.00	/	0.20
AF09B	Novigrad	B	0.10 - 0.50	/	0.13
AF10B	Zadar	B	0.10 - 0.50	/	0.17
AF11B	Dugi Otok	B	0.10 - 0.50	/	0.19
AF12B	Imotski	B	0.10 - 0.70	/	0.17
AF13B	Hvar	B	0.10 - 0.70	4.20 - 5.00	0.39
AF14B	Vis-Korčula	B	0.10 - 0.50	4.20 - 5.00	0.23
AF15C	Eastern Adriatic offshore	C	0.15 - 0.50	/	0.13
AF16C	Jana-1	C	0.10 - 0.50	/	0.09
AF17C	Palagruža	C	0.10 - 0.50	/	0.14
AF18B	Metković	B	0.10 - 0.80	4.20 - 5.00	0.28
AF19B	Mljet	B	0.15 - 1.00	4.20 - 5.00	0.13
AF20B	Montenegro offshore	B	0.15 - 1.00	/	0.73

m/yr)		
FEM Modeled		Composite solution
Max	Average	
0.12	0.04	0.02 - 1.00
0.07	0.04	0.03 - 0.50
0.22	0.10	0.06 - 0.50
0.27	0.08	0.05 - 0.50
0.34	0.13	0.08 - 0.50
0.53	0.15	0.08 - 0.53
0.62	0.24	0.10 - 0.62
0.61	0.37	0.10 - 1.00
0.52	0.25	0.10 - 0.52
0.52	0.30	0.17 - 0.52
0.60	0.36	0.10 - 0.60
0.65	0.34	0.10 - 0.70
1.69	0.98	0.10 - 4.20
0.50	0.38	0.10 - 4.20
0.20	0.17	0.13 - 0.50
0.14	0.12	0.09 - 0.50
0.22	0.18	0.10 - 0.50
1.63	0.89	0.10 - 4.20
1.76	0.97	0.15 - 4.20
2.88	2.01	0.15 - 2.88

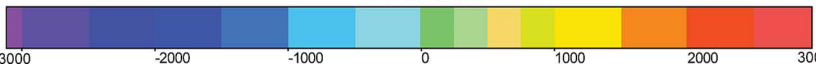


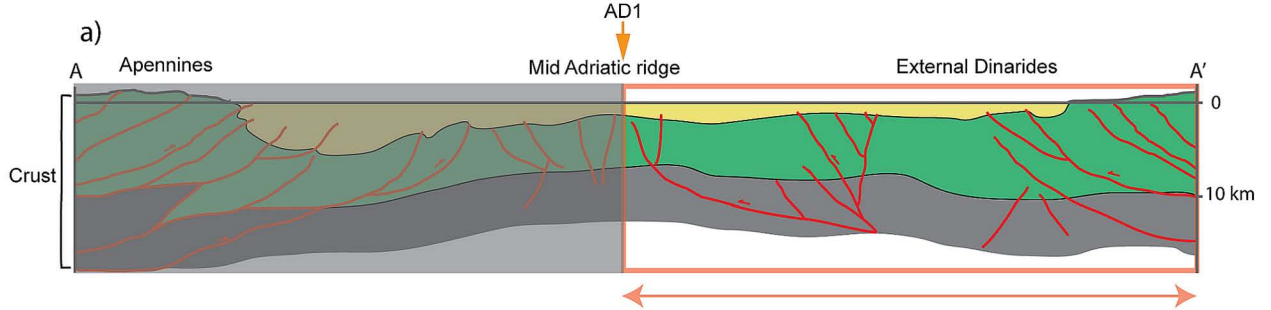
WSM08 SHmax direction and stress regime:

- NF
- NS
- SS
- TS
- TF
- U



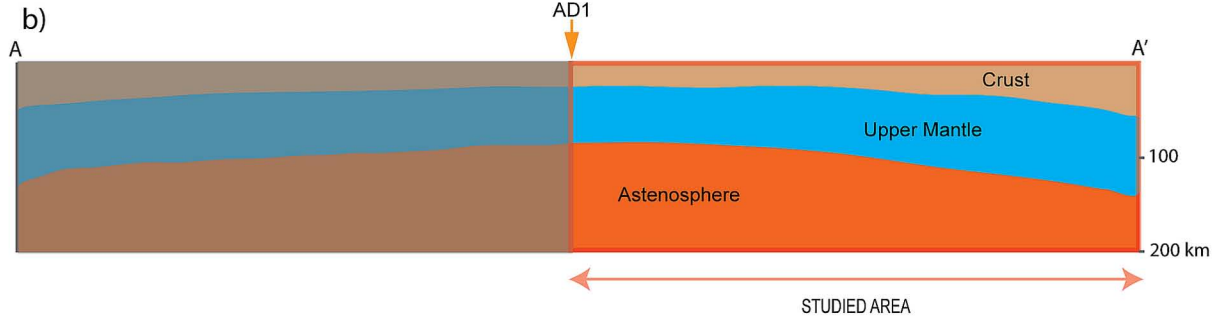
13° 14° 15° 16° 17° 18° 19° 20°

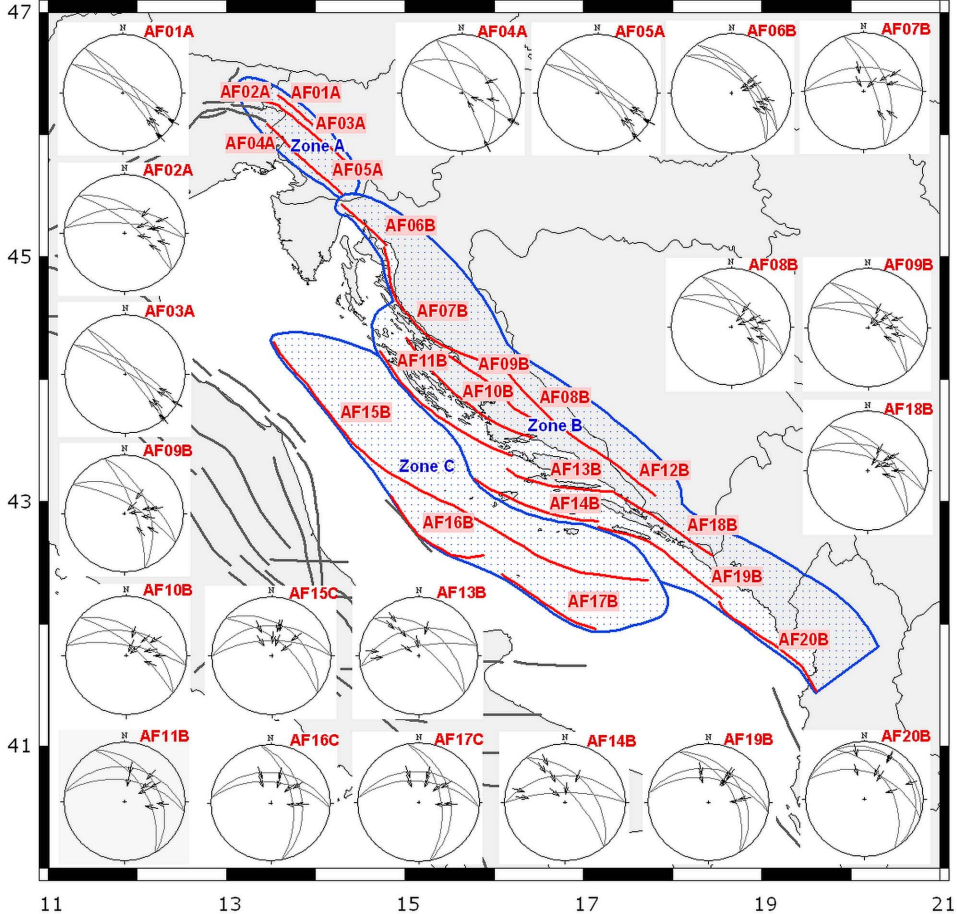


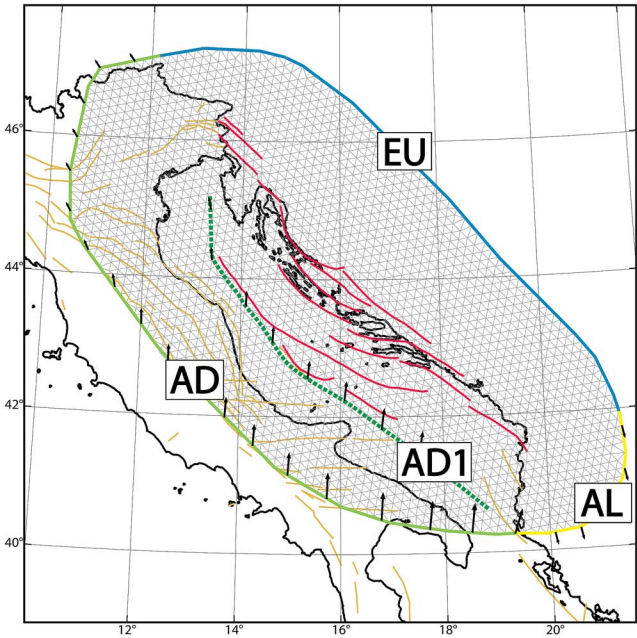


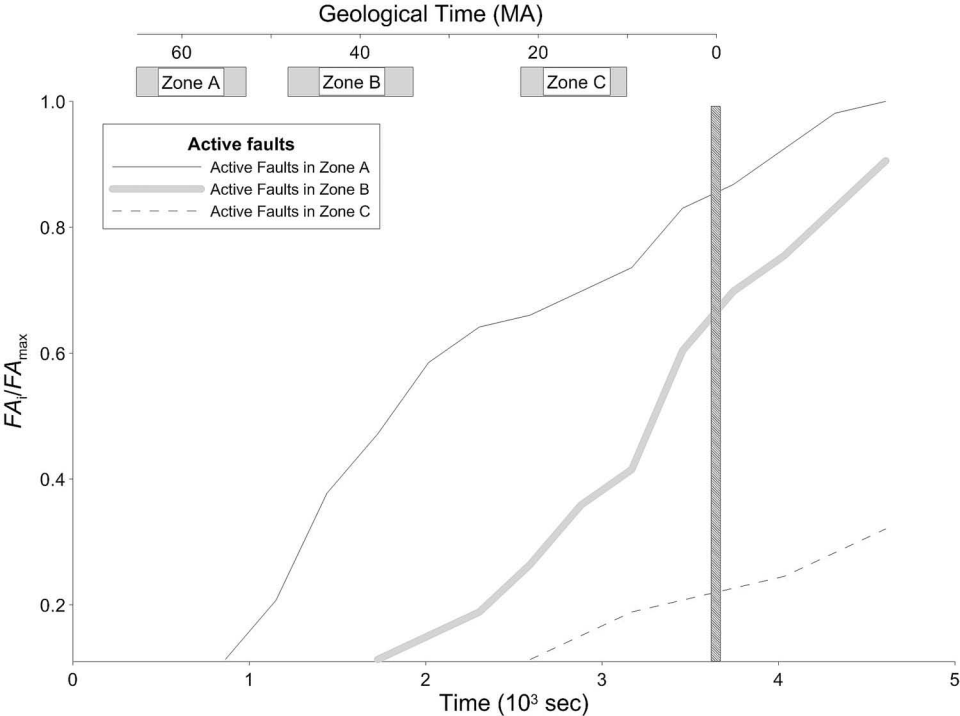
Tertiary and Quaternary foredeep clastic rocks and sediments
 Mesozoic platform and basin carbonates
 Variscan basement

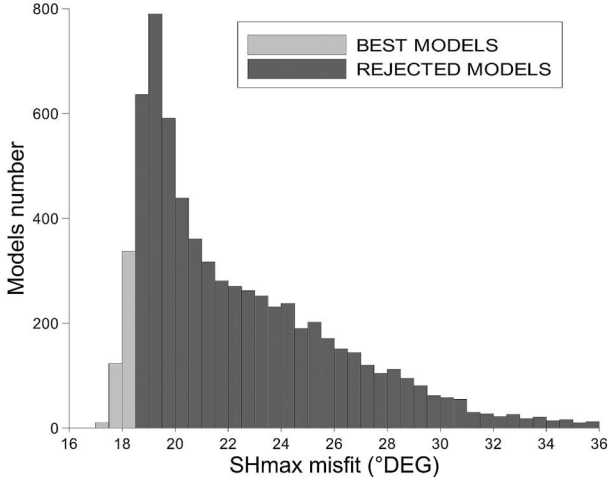
fault
 stratigraphic boundary
 topography



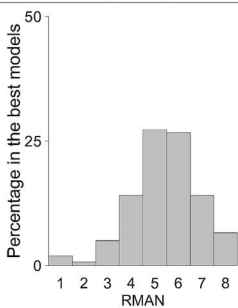




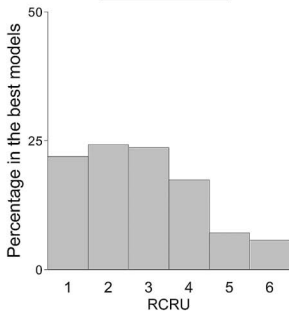


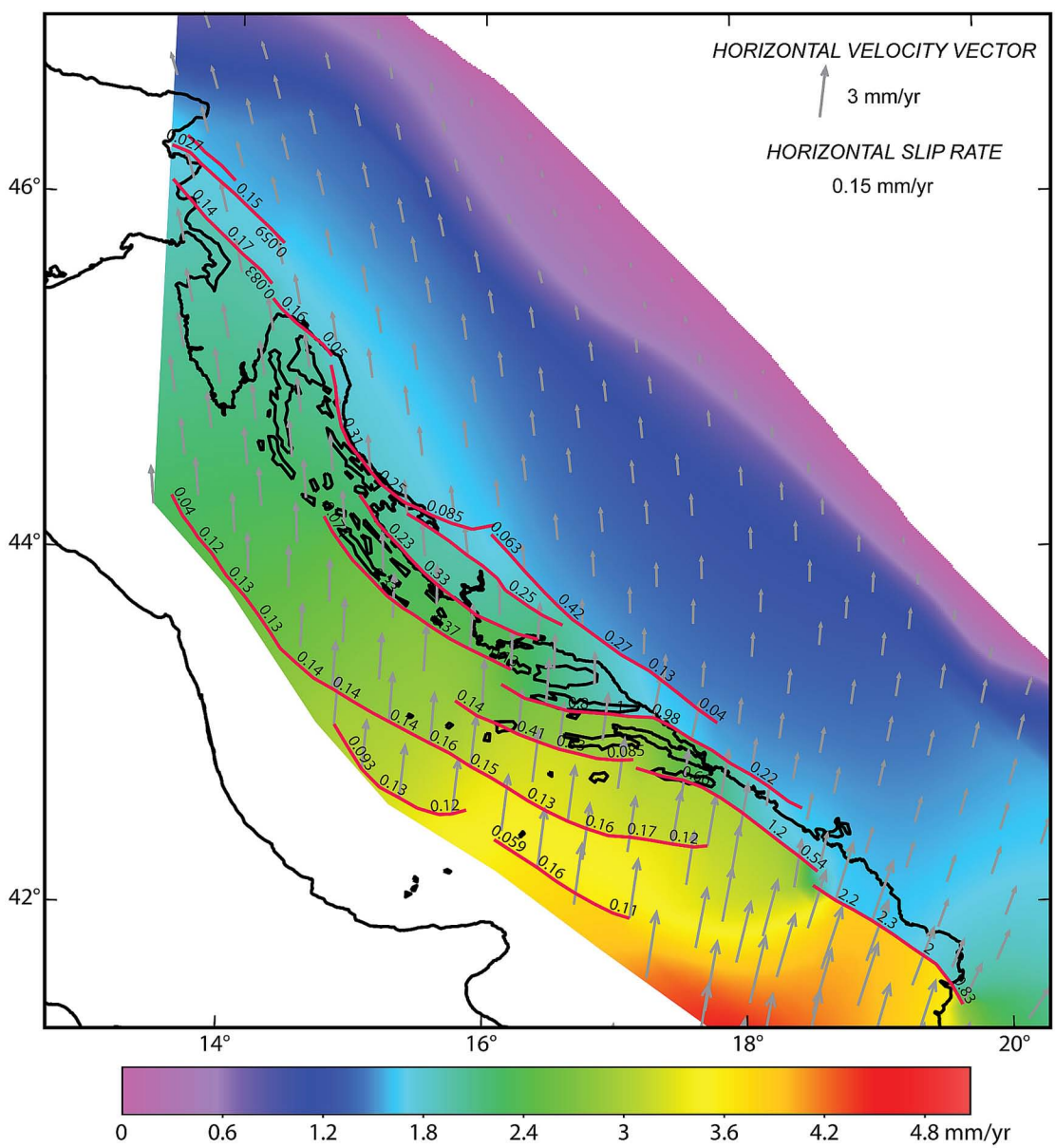


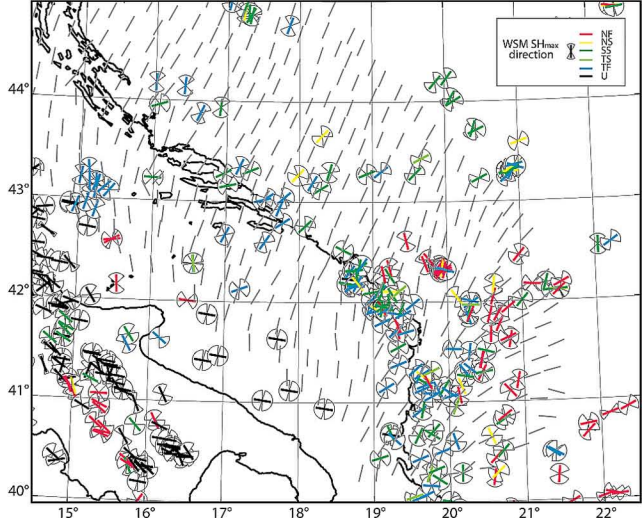
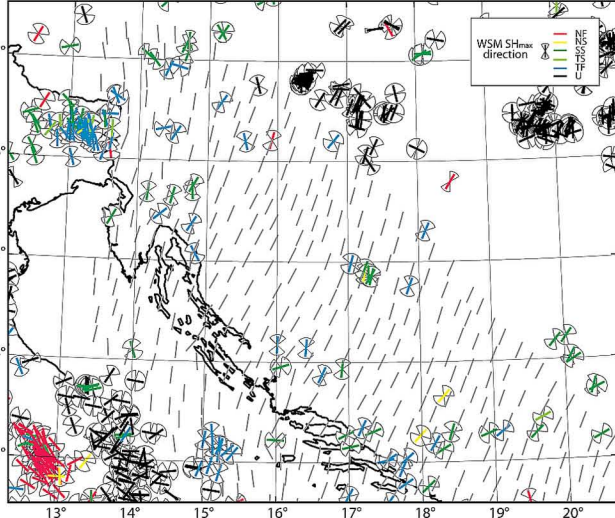
Lithosphere Upper Mantle Rheology (RMAN)



Crust Rheology (RCRU)







AF05 - active fault code

0.14 (mm/yr) - fault slip rate

kinematics:

thrust

dextral ss

